



LACOSTE: Exploiting stereo and temporal contexts for surgical instrument segmentation

Qiyuan Wang^{a,b}, Shang Zhao^{a,b}, Zikang Xu^{a,b}, S Kevin Zhou^{a,b,c,d,*}

^aSchool of Biomedical Engineering, Division of Life Sciences and Medicine, University of Science and Technology of China (USTC), Hefei Anhui, 230026, China

^bCenter for Medical Imaging, Robotics, Analytic Computing & Learning(MIRACLE), Suzhou Institute for Advanced Research, USTC, Suzhou, Jiangsu, 215123, China

^cKey Laboratory of Precision and Intelligent Chemistry, USTC, Hefei Anhui, 230026, China

^dKey Lab of Intelligent Information Processing of Chinese Academy of Sciences(CAS), Institute of Computing Technology, CAS, Beijing, 100190, China

arXiv:2409.09360v2 [cs.CV] 30 Sep 2024

ARTICLE INFO

Article history:

Keywords: Surgical data science, Stereo-temporal modeling, Set classifier, Query-based segmentation, Transformer

ABSTRACT

Surgical instrument segmentation is instrumental to minimally invasive surgeries and related applications. Most previous methods formulate this task as single-frame-based instance segmentation while ignoring the natural temporal and stereo attributes of a surgical video. As a result, these methods are less robust against the appearance variation through temporal motion and view change. In this work, we propose a novel **LACOSTE** model that exploits **Location-Agnostic CO**ntexts in **S**tereo and **TE**mporal images for improved surgical instrument segmentation. Leveraging a query-based segmentation model as core, we design three performance-enhancing modules. Firstly, we design a disparity-guided feature propagation module to enhance depth-aware features explicitly. To generalize well for even only a monocular video, we apply a pseudo stereo scheme to generate complementary right images. Secondly, we propose a stereo-temporal set classifier, which aggregates stereo-temporal contexts in a universal way for making a consolidated prediction and mitigates transient failures. Finally, we propose a location-agnostic classifier to decouple the location bias from mask prediction and enhance the feature semantics. We extensively validate our approach on three public surgical video datasets, including two benchmarks from EndoVis Challenges and one real radical prostatectomy surgery dataset GraSP. Experimental results demonstrate the promising performances of our method, which consistently achieves comparable or favorable results with previous state-of-the-art approaches.

© 2024 Elsevier B. V. All rights reserved.

1. Introduction

Computer-assisted intervention (CAI) has emerged as a transformative force in surgical procedures as it enhances patient safety, improves operative quality, reduces adverse event, and shortens recovery period (Maier-Hein et al., 2017). In this context, achieving semantic and instance segmentation of a surgical scene, as captured by surgical stereo cameras, plays a crit-

ical role in modern CAI systems. Semantic annotations enable cognitive assistance by providing pixel-wise contextual awareness of instruments, which is essential for supporting various downstream tasks, including surgical decision-making (Loftus et al., 2020; Maier-Hein et al., 2022), surgical navigation (Allan et al., 2020), and skill assessment (Curtis et al., 2020; Liu et al., 2021). Accurately identifying instruments and their spatial locations is a key focus in CAI, encompassing endeavors such as tool pose estimation (Hein et al., 2021), tool tracking and control (Du et al., 2019), and surgical task automation (Nagy and

*Corresponding author: Email: skevinzhou@ustc.edu.cn

Haidegger, 2019). Moreover, the integration of surgical scene contexts can facilitate selective overlaying of different objects within augmented reality environments, opening new possibilities for the next generation of surgical education (Allan et al., 2020).

Consequently, there is a growing need for automated segmentation of surgical instruments, prompting active research in this domain. However, achieving precise instance segmentation from surgical videos confronts significant challenges. Complicated surgical scenes exhibit a low inter-class variance, such as variations between different instruments, and a high intra-class variance, such as instances of dynamic posed instruments. Class imbalance is also prevalent in surgical scenes, with the identification of small objects and rarely used instruments proving to be difficult. Challenges further arise from motion blur, lighting changes, and occlusions caused by smoke and blood (Bouget et al., 2017). In recent years, remarkable progress has been made in the development of semantic and instance segmentation algorithms within the surgical community. While notable strides have been made in addressing this challenge, there are still some specific challenges that necessitate further improvement. Addressing these challenges represents crucial avenues for future research, aiming to advance instrument segmentation techniques and foster a more comprehensive understanding of surgical scenes (Wei et al., 2022). This constitutes the focus of this paper, that is, improving the performance of **surgical instrument segmentation (SIS)**.

For SIS, the effectiveness of query-based segmentation (QBS) methods has been validated by previous works. The findings of (Baby et al., 2023) indicate that instrument misclassification primarily leads to low performance of current SIS methods. While most methods yield satisfactory results in terms of both the bounding box and segmentation mask, they frequently misclassify the output box or mask. Therefore, we follow the QBS paradigm and derive our method, grounded on three limitations of current methods, to mitigate instrument misclassification for surgical scenario. Firstly, surgical frames are recorded by stereo cameras and have inherent stereo attributes that are largely ignored by previous works. The complementary depth-aware information from stereo frame can enhance current view features, which help instrument localization and recognition for complex scenes. From this, we design a *disparity-guided feature propagation* (DFP) module, which integrates features from stereo views with an offline disparity estimation network explicitly. DFP can be inserted into QBS baseline without additional trainable parameters. To generalize well to a monocular setting, we also propose a pseudo stereo mechanism, which generates complementary right frames within multiple disparity ranges. Some examples are illustrated in Figure 3.

Secondly, most QBS methods for SIS group image pixels into different segments including binary masks and corresponding instrument categories from only frame-wise information. However, the appearance of instruments across temporal and stereo frames exhibits great variations due to motion blur, occlusion, and so on. Hence, we address SIS from a tracklet perspective and propose a *stereo-temporal set classifier* (STSCls), which decides the final instrument category of each segment

after aggregating instrument information through a stereo clip. A tracklet means a short track of instance across frames. In this paper, we extend the tracklet definition to *a set of object query embeddings corresponding to the same identity across temporal and stereo dimensions*, wherein each item of tracklet represents an object query embedding. Since STSCls takes stereo-temporal contexts within a tracklet into account for each instrument segment, it is robust against temporal shifts and view changes and avoids a collapse of final predictions from transient failures. STSCls can be cascaded on top of QBS baseline and trained jointly with tracklets generated from QBS outputs. Given the absence of video instance annotations for most surgical datasets, we design a query alignment mechanism and identity alignment loss to align identity IDs based on query indexes instead of an additional track head for tracklets generation. Due to the generality of these mechanisms, STSCls can be extended to train with various tracklet configurations including stereo clip and monocular clip.

Finally, binary mask and instrument category of each segment for QBS methods are originated from the same object query (embedding). The embeddings learn not only semantic contents but also location biases, which can make them scattered into different clusters in semantic feature space and hence have a negative influence for classification. In fact, the features used for segmentation are not necessarily appropriate for classification. To this end, we propose an additional *location-agnostic classifier* (LACls) to decouple the location bias from semantic information. With a plug-and-play design, this classifier can be easily plugged on top of QBS architecture. In this work, LACls receives the mask prediction from QBS baseline and cropped images to extract features. The features of location-agnostic structure are clustered compactly within the same category.

We extensively evaluate our method on three publicly available surgical datasets, including two benchmarks from EndoVis Challenges together with one real radical prostatectomy surgery dataset GraSP and demonstrate that our new approach achieves comparable or favorable results with existing state-of-the-art (SOTA). Our main contributions are:

1. We propose a novel query-based segmentation framework, **LACOSTE**, which jointly exploits Location-Agnostic COntexts in Stereo and TEmporal images for improved surgical instrument segmentation.
2. We design a disparity-guided feature propagation (**DFP**) module to enhance current feature with stereo cue, a stereo-temporal set classifier (**STSCls**) to improve semantic inference with temporal-stereo context, and a cascaded location-agnostic classifier (**LACls**) to mitigate the negative influence of location bias for classification.
3. We develop a query alignment mechanism and identity alignment loss to promote instance consistency across frames in one stereo clip instead of a track head.
4. Our method achieves performance gains in three open benchmark datasets when compared with prior state-of-the-art methods.

2. Related Work

CNN-based SIS. Initial efforts in surgical robotics community are based on Convolutional Neural Networks (CNNs). For instance, TernausNet (Shvets et al., 2018) proposes a pretrained U-Net (Ronneberger et al., 2015) model for the segmentation of a restricted variety of surgical instruments. U-NetPlus modifies a U-Net architecture and data augmentation strategies to improve performance (Hasan and Linte, 2019). PAANet pays more attention to multi-scale attentive features (Ni et al., 2020). To improve the segmentation results, some researchers incorporate additional priors such as optical flow and motion cue (Zhao et al., 2020; Jin et al., 2019), stereoscopic information (Mohammed et al., 2019), or saliency maps (Islam et al., 2019). These previous models formulate SIS as a single frame per-pixel classification task, which often produces disconnected areas and ignores a multi-instance nature. Some works have argued for formulating the task as multi-class instance segmentation in a single frame. ISINet (González et al., 2020) applies a Mask-RCNN (He et al., 2017) accompanied with optical flow to address instance-based instrument segmentation. S3Net (Baby et al., 2023) analyzes the low-IoU performance of previous methods and pays more attention to classification. Specially, it applies a mask-based attention and contrastive loss to address the variation in aspect ratio and inter-class appearance similarity.

Transformer-based SIS. In recent years, Vision Transformers (ViTs) (Liu et al., 2022; Dosovitskiy et al., 2020) have emerged as the leading models in diverse computer vision tasks, showcasing their state-of-the-art performance. Among these works, query-based segmentation architectures like MaskFormer (Cheng et al., 2021), which utilize a fixed-size set of learnable object queries to predict regions, have tremendous advantages for universal segmentation tasks. The effectiveness of treating instance segmentation as a joint problem of mask segmentation and mask classification has been validated in many segmentation tasks. Inspired from these works, some researchers introduce Transformers into SIS task. In this regard, (Sun et al., 2022) is the first to integrate Transformers into instrument segmentation by combining CNNs with Swin Transformers as backbone. (Dhanakshiru et al., 2023) reveal that incorrect query initialization limits the effectiveness of current query-based methods and propose a class-agnostic Query Proposal Network (QPD) to improve query initialization.

Temporality-enhanced SIS. Temporal attributes have been taken into account in SIS tasks. Previous CNN-based approaches often incorporate optical flow information without fully exploiting global video contexts. Compared with CNN-based methods, video Transformers have advantages of aggregating long-term video reasoning and showcase their superior performance in video tasks. TraSeTr (Zhao et al., 2022) is a track-to-segment Transformer that dynamically integrates tracking cues to assist instance-level surgical instrument segmentation. STSwinCL (Jin et al., 2022) employs a video Swin Transformer with a contrastive learning approach for panoptic segmentation of surgical scenes in videos. TAPIR (Valderrama et al., 2022) introduces a video Transformer-based model for multi-level surgical workflows analysis accompanied with De-

formable DETR (Zhu et al., 2020) for instrument detection, offering an improved solution for SIS. TAPIS (Ayobi Mendoza, 2023) is a multi-task transformer-based architecture that combines a global video feature extractor with a localized region proposal network for actions, phases, steps recognition and instrument segmentation. CaRTS (Ding et al., 2023) introduces temporal constraints on kinematics data for counterfactual surgical segmentation. MATIS (Ayobi et al., 2023) utilizes pixel-wise attention for targeting instrument areas and video transformers for temporal information.

Set Classifier. Recently, it has been shown that making a consolidated decision from multiple frames is beneficial to improve the quality of detection and segmentation in natural scene (Bertasius and Torresani, 2020; Hwang et al., 2021; Ke et al., 2021). SCTTrack (Hwang et al., 2022) first pays more attention to using set classifier to improve the classification performance. SCTTrack uses a track head to compose boxes tracklets dynamically and use set classifier with region proposals features to predict the final results of instances. The effectiveness of this structure is based on extensive region proposals that explain the same instance from different views generated by Region Proposal Network module and sequence generation strategy.

3. Query-Based Segmentation

3.1. QBS Preliminaries

The QBS method partitions image pixels into N segments by predicting N binary masks and N corresponding category labels, where N is significantly larger than the real segment number \tilde{N} . QBS represents each segment with a feature vector (“object query embedding”) which can be processed into category label and binary mask. The key challenge is to find good representations for each segment. For simplicity, we term object query embedding as object query in the following. As concluded in (Cheng et al., 2021), a meta QBS architecture would be composed of three components: backbone, pixel decoder, and Transformer decoder together with trainable queries.

Given an image I , the backbone θ first extracts low-resolution features. Then, the pixel decoder δ that gradually upsamples low-resolution features from the backbone to generate high-resolution per-pixel features F . Finally, the Transformer decoder ζ together with N initial learnable query embeddings $Q = \{q_n\}_{n=1}^N$ operates on image features to process N object query embeddings $\{e_n\}_{n=1}^N$. The final predictions of N segments are a set of N probability-embedding-mask pairs $z = \{(p_n, e_n, m_n)\}_{n=1}^N$, where the probability distribution p_n contains C classes and an auxiliary “no object” label (\emptyset) to denote segments that do not correspond to any classes; e_n is object query embedding to represent segment, where n means query index; and m_n is binary mask. The object query assigned with “no object” label is termed as a *non-object query*. In this research, we **formulate each segment as instance and merge the selected instances into one semantic segmentation map**. The overall pipeline can be illustrated in Figure 1.

The training losses are composed of classification and binary segmentation parts as represented in Eq. (1), where λ_{bce} , λ_{dice}

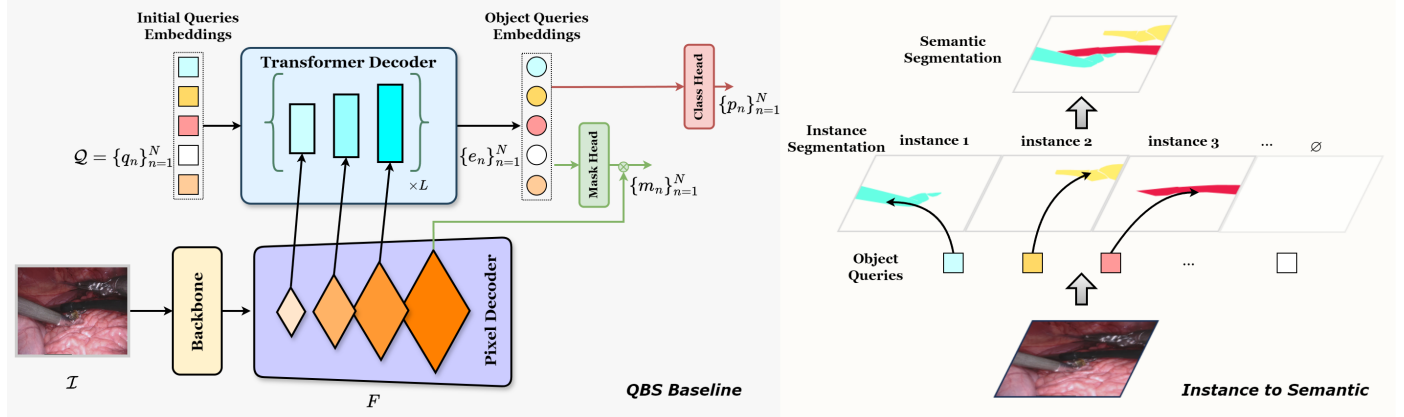


Fig. 1. Schematic illustration of Query-Based Segmentation architecture. The key components include backbone encoder, pixel decoder and transformer decoder together with learnable queries(embeddings).

Table 1. The mathematical symbols in this work.

QBS			Frame Step			Tracklet Step		
Notions	Details	Description	Notions	Details	Description	Notions	Details	Description
\mathcal{I}		input image	$\mathcal{I}^{\mathcal{L}}$		left view	s	$\{s_n\}_{n=1}^N$	tracklets
F		pixel-wise features	$\mathcal{I}^{\mathcal{R}}$		right view	p^s	$\{p_n^s\}_{n=1}^N$	class probability
n		query index	t		frame index	e^s	$\{e_n^s\}_{n=1}^N$	object query
N		queries number	t^*		current time			
\tilde{N}		real instance number	T		clip length			
p	$\{p_n\}_{n=1}^N$	class probability	C	$\{(\mathcal{I}^{\mathcal{L}}(t), \mathcal{I}^{\mathcal{R}}(t))\}_{t=1}^T$	stereo clip	p^a	$\{p_n^a\}_{n=1}^N$	class probability
m	$\{m_n\}_{n=1}^N$	binary mask	p^b	$\{p_n^b\}_{n=1}^N$	class probability	e^a	$\{e_n^a\}_{n=1}^N$	object query
e	$\{e_n\}_{n=1}^N$	object query	m^b	$\{m_n^b\}_{n=1}^N$	binary mask			
Q	$Q = \{q_n\}_{n=1}^N$	initial query	e^b	$\{e_n^b\}_{n=1}^N$	object query			
z	$z = \{(p_n, e_n, m_n)\}_{n=1}^N$	prediction outputs						
\tilde{z}	$\tilde{z} = \{(\tilde{c}_n, \tilde{m}_n)\}_{n=1}^{\tilde{N}}$	ground truth						

and λ_{cls} are weighted hyper-parameters. Hungarian matching makes instances matching between the predictions and ground truths $\tilde{z} = \{(\tilde{c}_n, \tilde{m}_n)\}_{n=1}^{\tilde{N}}$ (\tilde{c}_n/\tilde{m}_n means class/binary mask ground truth). The cross entropy (**CE**) loss \mathcal{L}_{cls} is applied for classification. For binary segmentation, the joint losses include binary cross entropy (**BCE**) loss \mathcal{L}_{bce} and the Dice loss \mathcal{L}_{dice} .

$$\begin{aligned} \mathcal{L}_{cls} &= \sum_{n=1}^N \text{CE}(p_n, \tilde{c}_n), \\ \mathcal{L}_{bce} &= \sum_{n=1}^{\tilde{N}} \text{BCE}(m_n, \tilde{m}_n), \mathcal{L}_{dice} = \sum_{n=1}^{\tilde{N}} \text{Dice}(m_n, \tilde{m}_n), \\ \mathcal{L}_{baseline} &= \lambda_{bce} \mathcal{L}_{bce} + \lambda_{dice} \mathcal{L}_{dice} + \lambda_{cls} \mathcal{L}_{cls}. \end{aligned} \quad (1)$$

3.2. Limitations of Current QBS

However, the original QBS framework *does* have limitations when applied to the SIS tasks. Firstly, current methods for SIS disregard additional information from stereo view which can enhance the precision of instrument localization and recognition. Secondly, prior studies typically focus on frame-wise predictions, neglecting the temporal characteristics of surgical videos, thereby leading to transient failures. Finally, QBS methods derive binary mask and instrument category of each segment from the same object query, wherein inherent location bi-

ases detrimentally impact instrument recognition. These limitations motivate us to propose the LACOSTE model, which follows the QBS paradigm (Mask2Former) and improves the effectiveness of current SIS works accompanied with three proposed modules including DFP, STSCls and LACls.

4. The LACOSTE Method

4.1. The Three Inference Steps

LACOSTE adheres to the QBS paradigm in conjunction with three proposed modules: DFP, STSCls, and LACls. The overall inference pipeline of LACOSTE can be divided into three steps which aim to enhance mask **classification** ability from various perspectives as illustrated in Figure 2. For **Frame Step**, the QBS baseline with DFP (termed as **BDFP**) explores depth-aware information from stereo views and makes frame-wise prediction for each timestamp. For **Tracklet Step**, STSCls aggregates temporal or stereo contexts contained in tracklets which are composed of object queries from frame step and makes a consolidated tracklet prediction. For **L-Agnostic Step**, LACls extracts instrument content information decomposed with location biases and predicts a location-agnostic prediction. The **ensemble** results from three steps replace original QBS classification results as the final classification predictions and final binary mask predictions keep same as those from frame step.

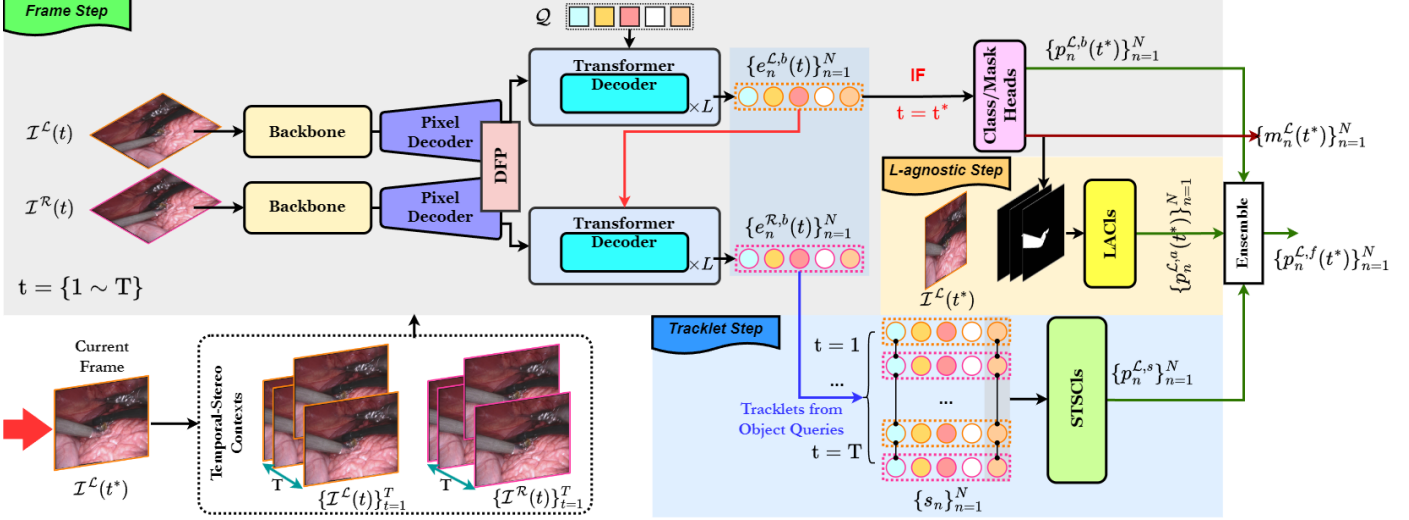


Fig. 2. Schematic illustration of an overview pipeline of our LACOSTE method. Specifically, the prediction flow is divided into Frame step, Tracklet step, and L-Agnostic step. Together with proposed DFP, STSCls and LACls, all steps improve SIS from different perspectives.

We define some mathematical notions in Table 1 and formulate the inference process of LACOSTE for current frame $I^L(t^*)$ as Algorithm 1. The upper suffix for three steps and final outputs are represented by b , s , a and f , respectively. Given a current frame $I^L(t^*)$ within a stereo clip $\{(I^L(t), I^R(t))\}_{t=1}^T$ (where t^* means current time, T means clip length, $t^* \in [1, T]$), LACOSTE goes through three steps and outputs the final segmentation results as follow.

◊ **Frame Step.** For each timestamp, BDFP receives a pair of stereo frames $(I^L(t), I^R(t))$ and derives the frame-wise predictions. Query alignment operation is applied to align identities across different timestamps. As shown in Eq. (2), BDFP outputs probability-embedding-mask pairs at current time t^* while it outputs only object query embeddings at other timestamps.

$$\left\{ \begin{array}{ll} \bigcup_{\mathcal{L}, \mathcal{R}} \{(e_n^b(t), p_n^b(t), m_n(t))\}_{n=1}^N & , \quad t = t^*, \\ \bigcup_{\mathcal{L}, \mathcal{R}} \{(e_n^b(t))\}_{n=1}^N & , \quad t \neq t^*. \end{array} \right. \quad (2)$$

◊ **Tracklet Step.** We collect object queries through a stereo clip from frame step and generate tracklets $\{s_n\}_{n=1}^N$ (where $s_n = \{(e_n^{b, \mathcal{L}}(t), e_n^{b, \mathcal{R}}(t))\}_{t=1}^T$) based on query index n . STSCls receives tracklets and makes tracklet-level class prediction $\{(e_n^s, p_n^s)\}_{n=1}^N$.

◊ **L-Agnostic Step.** LACls receives processed images based on binary masks $\{m_n^L(t^*)\}_{n=1}^N$ from frame step and outputs location-agnostic predictions $\{(e_n^a(t^*), p_n^a(t^*))\}_{n=1}^N$.

The final outputs of LACOSTE for current frame are composed of binary masks $\{m_n^L(t^*)\}_{n=1}^N$ and corresponding class predictions $\{p_n^{f, \mathcal{L}}(t^*)\}_{n=1}^N$. The class predictions are ensemble with frame class prediction p^b , tracklet class prediction p^s and location-agnostic class prediction p^a . Considering the outputs of the Frame step are utilized in the other two steps, LACOSTE first performs the Frame step and subsequently executes the

Algorithm 1 LACOSTE Inference Algorithm

Input: Current Frame/Time $I^L(t^*)/t^*$, Corresponding Stereo Clip $\{(I^L(t), I^R(t))\}_{t=1}^T$, Clip Length T , Ensemble Weighted Parameters α_b , α_s , and α_a .

Params: BDFP Φ_B , STSCls Φ_S , LACls Φ_A , Initial Queries Q .

Output: Segmentation results $S(t^*) = \{(p_n^f(t^*), m_n^f(t^*))\}_{n=1}^N$.

Frame Step

```

1: for  $t \leftarrow 1$  to  $T$  do
2:   if  $t > 1$  then
3:      $Q = \{e_n^{b, \mathcal{L}}(t-1)\}_{n=1}^N$                                 ▷ Query Alignment
4:   else
5:      $Q = \{q_n\}_{n=1}^N$ 
6:   end if
7:   if  $t = t^*$  then
8:      $\Phi_B(I^L(t), I^R(t)) \xrightarrow{Q} \bigcup_{\mathcal{L}, \mathcal{R}} \{(e_n^b(t), p_n^b(t), m_n(t))\}_{n=1}^N$ 
9:   else
10:     $\Phi_B(I^L(t), I^R(t)) \xrightarrow{Q} \bigcup_{\mathcal{L}, \mathcal{R}} \{(e_n^b(t))\}_{n=1}^N$ 
11:  end if
12: end for

```

Tracklet Step

Generate tracklets $\{s_n\}_{n=1}^N$ from object queries, where $s_n = \{(e_n^{b, \mathcal{L}}(t), e_n^{b, \mathcal{R}}(t))\}_{t=1}^T$

```

13: for  $n \leftarrow 1$  to  $N$  do
14:    $\Phi_S(s_n) \rightarrow (e_n^s, p_n^s)$ 
15: end for

```

L-Agnostic Step

```

16:  $\Phi_A(I^L(t^*), \{m_n^L(t^*)\}_{n=1}^N) \rightarrow \{(e_n^a(t^*), p_n^a(t^*))\}_{n=1}^N$ 

```

Final Results

binary mask $m_n^f(t^*) = m_n(t^*)$

class prediction $p_n^f(t^*) = \alpha_b p_n^b(t^*) + \alpha_s p_n^s + \alpha_a p_n^a(t^*)$

return $S(t^*) = \{(p_n^f(t^*), m_n^f(t^*))\}_{n=1}^N$.

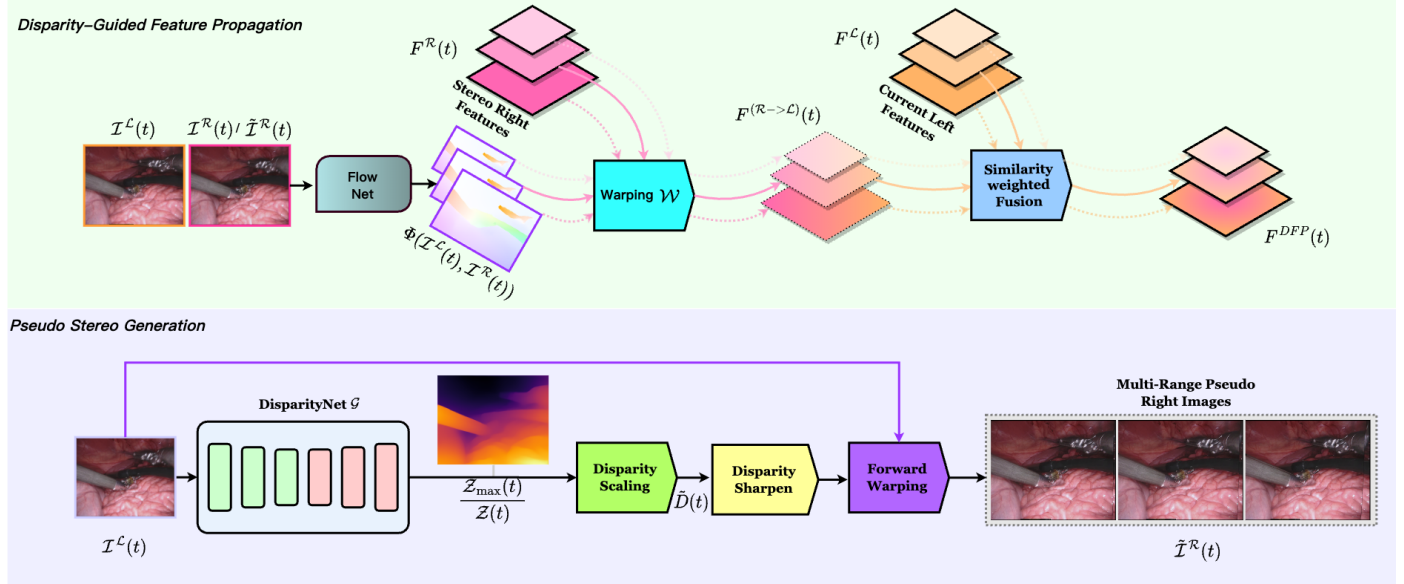


Fig. 3. Schematic illustration of our DFP module and pseudo stereo generation mechanism. DFP fuses complement information from stereo pairs at feature level. Pseudo stereo generation mechanism generates virtual multi-range right images for only monocular dataset.

Tracklet and L-Agnostic steps in parallel. We will elaborate all three modules and training losses in the following sub-sections.

4.2. Disparity-Guided Feature Propagation (DFP)

DFP Structure & Formulation. As presented in the top row of Figure 3, DFP makes a bridge to exploring stereo information at feature level inspired by temporal tasks (Zhao et al., 2022; Zhu et al., 2017). It converts the stereo right features to current left features guided with an offline flow estimation model and fuses weighted pair features adaptively. Without inducing additional trainable parameters, this operation can enhance current left features with stereo right features. Specifically, LACOSTE first extracts high-resolution per-pixel feature maps ($F^L(t), F^R(t)$) for a given stereo pair ($I^L(t), I^R(t)$), respectively. An offline optical-flow network Φ is introduced to estimate disparity between stereo frames. The DFP module applies a backward warping function \mathcal{W} to make the stereo features $F^R(t)$ aligned with the current features $F^L(t)$. After that, the warped stereo features are fused adaptively with current features. The below equations represent this operation.

$$F^{(R \rightarrow L)}(t) = \mathcal{W}(F^R(t), \Phi(I^L, I^R)), \quad (3)$$

$$F^{DFP}(t) = F^L(t) + w^{(R \rightarrow L)} F^{(R \rightarrow L)}(t), \quad (4)$$

where the weight $w^{(R \rightarrow L)}$ is the pixel-wise cosine similarities between the warped stereo features $F^{(R \rightarrow L)}(t)$ and the current left features $F^L(t)$. The DFP enhancement features $F^{DFP}(t)$ are delivered to the next transformer decoder of QBS baseline instead of original monocular ones. We train BDFP via the original losses $\mathcal{L}_{baseline}$ represented as Eq. (1).

Pseudo Stereo Generation. To exploit the stereo cues for even monocular surgical dataset, we apply a pseudo stereo generation mechanism to complement pseudo right images inspired by (Watson et al., 2020). As shown in the bottom row of

Figure 3, we apply an offline monocular depth network \mathcal{G} to estimate the depth $Z(t) = \mathcal{G}(I^L(t))$ for left frame $I^L(t)$. The disparities $\tilde{D}(t)$ are translated from estimated depth and scaled by a random scaling factor d_s within a plausible range $[d_{min}, d_{max}]$ as reported in Eq. (5). The scaling factor d_s simulates different camera baseline and focal length. After that, we use a forward warping operation \mathcal{F} to obtain every pixel of pseudo right view $\tilde{I}^R(t)$ from corresponding left view $I^L(t)$. Eq. (6) symbolizes this operation.

$$\tilde{D}(t) = d_s \frac{Z_{max}(t)}{Z(t)}, \quad (5)$$

$$\tilde{I}^R(t) = \mathcal{F}(\tilde{D}(t), I^L(t)). \quad (6)$$

Different from previous methods (Watson et al., 2020) that supplement stereo information only in training time, we make simulation not only in training stage with a randomly-sampled scale factor but also in inference stage with an average scale factor. A series of strategies are also applied to handle the unrealistic nature of generated image $\tilde{I}^R(t)$. To address ‘blurry’ edges, a Sobel edge filter is used to identify the flying pixels and sharpen the disparity map. Instead of filling invisible regions with other images randomly sampled in (Watson et al., 2020), we fill the missing regions with textures from a temporal frame or keep blank value with a valid mask to relieve the effect of noise for the DFP module.

4.3. Stereo-Temporal Set Classifier (STSCls)

Forming tracklets from object queries is the first step for STSCls to make tracklet-level prediction. However, it is difficult for most surgical datasets to get video identity annotations, which describe instance correlations among frames. The naive tracklet sampling mechanism or training a track head is unrealizable for missing identity IDs. How to label pseudo identity ID for each object query by exploring temporal and stereo contexts is a major challenge for forming tracklets.

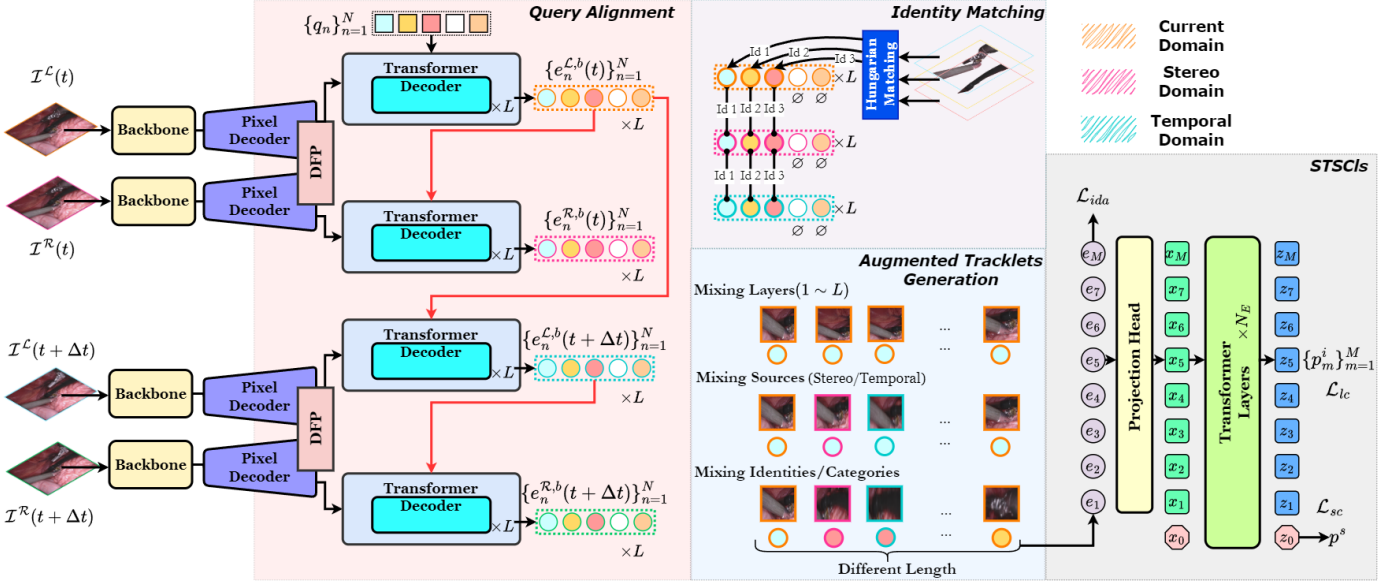


Fig. 4. Schematic illustration of our STSCls module & Training Pipeline.

How to generate pseudo identity ID for object queries?

Query Alignment. Considering that object queries are good representation for instances, they can make a bridge to align identities between frames. We present a simple but valid query alignment mechanism to align identity correlation across both temporal and stereo dimensions. As illustrated in “Query Alignment” section of Figure 4, given a pair of current frame $\mathcal{I}^L(t)$, stereo frame $\mathcal{I}^R(t)$, temporal frame $\mathcal{I}^L(t + \Delta t)$ and stereo temporal frame $\mathcal{I}^R(t + \Delta t)$, we replace the initial learnable query embeddings Q of BDFP for temporal $\mathcal{I}^L(t + \Delta t)$ and stereo frame $\mathcal{I}^R(t)$ with object query embeddings of the current frame $\mathcal{I}^L(t)$. Then, we assume object queries with the same query index n can correspond to the same identity across **short-term** frames. From this, we can label pseudo identity ID of object query and sample tracklets based on query index n , which are easy to access.

How to select object queries for tracklets generation?

Identity Matching. After query alignment, we get pseudo identity ID of all object queries. However, given a large amount of object queries not corresponding to any instances (non-object queries), identity matching is necessary to filter out the invalid queries before tracklets generation, which reduces uncontrollable training noise. Specifically, valid object queries of current frame $\mathcal{I}^L(t)$ are selected by Hungarian Matching with annotations as described in the “Identity Matching” section of Figure 4. For consecutive temporal $\mathcal{I}^L(t + \Delta t)$ and stereo frames $\mathcal{I}^R(t)$, the corresponding ones with matched query indexes will also be maintained. The scheme can reduce training instability in some certain.

How to augment tracklets for training STSCls?

Augmented Tracklets Generation. After identity matching, the number of valid object queries is far smaller than region proposals of RPN. Instead of sampling tracklets only based on pseudo identity IDs, various tracklet augmentation methods are applied to mitigate overfitting. Firstly, the intermediate ob-

ject query embeddings from multi-layer Transformer decoder of BDFP have different perspectives to describe the same instance. From this, augmented tracklets can be produced by integrating intermediate object queries derived from various L Transformer decoder layers. Owing to the generality, the augmentation can be extended to temporal and stereo frames. Secondly, integrating object queries from different sources, including temporal sequences and stereo pairs, enhances the diversity further. Thirdly, object queries with various identities or categories are mixed through a tracklet, significantly increasing the number of potential tracklets. Finally, for mitigating the long-tail problems in surgery duration, we sample multi-length tracklets, following the distribution inversely proportional to category portions. The eponymous section of Figure 4 shows the process and gives some augmented examples.

STSCls Structure & Formulation. STSCls aims to aggregating instance information contained in a tracklet and making a consolidated prediction to improve single frame results. As illustrated in “STSCls” section of Figure 4, STSCls is composed of stacked N_E Transformer layers like (Hwang et al., 2022). Inputs for this module come from two sources: a trainable set classification token and instance tokens derived from a tracklet. Given a tracklet $s_k = \{e_{k,m}^b\}_{m=1}^M$ (where M means tracklet length, k means identity ID), a projection head first encodes embedding items into instance tokens $\{x_m\}_{m=1}^M$. By inserting the set classification token x_0 and instance tokens $\{x_l\}_{l=1}^L$ into STSCls, the set classification token x_0 aggregates the overall contextual information via self-attention operation from instance tokens. The output embeddings $\{z_l\}_{l=0}^M$ of STSCls are further processed into class predictions including a set classification logit p^s and local instance classification logits $\{p_m^i\}_{m=1}^M$. The former p^s represents tracklet-level class prediction. We define z_0 as *tracklet object query embedding* represented as \mathbf{e}^s in the following.

Training Losses. For training STSCls with augmented tracklets, we design a joint training loss composed of global

set classification loss \mathcal{L}_{sc} , local instance classification loss \mathcal{L}_{lc} and identity alignment loss \mathcal{L}_{ida} . The global set classification loss \mathcal{L}_{sc} is formulated as a typical cross entropy (**CE**) loss between set classification logit p^s and tracklet-level ground truth y_{gt}^s as Eq. (7). To accelerate the training process, the local instance classification loss \mathcal{L}_{lc} is applied to assist STSCls training with local instance classification logits $\{p_m^i\}_{m=1}^M$ and instance-level ground truths $\{y_{gt,m}^i\}_{m=1}^M$. The formulation is also a cross entropy loss as in Eq. (7).

$$\mathcal{L}_{sc} = \mathbf{CE}(p^s, y_{gt}^s), \mathcal{L}_{lc} = \sum_{m=1}^M \mathbf{CE}(p_m^i, y_{gt,m}^i). \quad (7)$$

From the assumption that object queries with the same identity ID should be similar, the identity alignment loss \mathcal{L}_{ida} lightly clusters the object query embeddings based on identities to assist queries alignment across stereo/temporal dimensions. In particular, we collect all K valid object queries after identity matching in a batch and calculate similarities \mathcal{M}^{sim} among them, where $m_{ij} \in \mathcal{M}^{sim}$ means the similarity of i_{th} and j_{th} object queries. The corresponding identity alignment ground-truths $\tilde{\mathcal{M}}$ measures whether any two object queries correspond to the same identity or not. The item $\tilde{m}_{ij} \in \tilde{\mathcal{M}}$ equals to 1 if i_{th} and j_{th} object queries share same identity ID and vice versa. The identity alignment loss Eq. (8) is set as a binary cross entropy (**BCE**) loss. As represented in Eq. (9), the overall training loss \mathcal{L}_{STSCls} is a combination of \mathcal{L}_{sc} , \mathcal{L}_{lc} , and \mathcal{L}_{ida} .

$$\mathcal{L}_{ida} = \sum_{i=1}^K \sum_{j=1}^K \mathbf{BCE}(m_{ij}, \tilde{m}_{ij}). \quad (8)$$

$$\mathcal{L}_{STSCls} = \mathcal{L}_{sc} + \mathcal{L}_{lc} + \mathcal{L}_{ida}. \quad (9)$$

4.4. Location-Agnostic Classifier (LACls)

LACls explicitly decouples mask classification with mask segmentation process to mitigate the adverse influence of location biases. This module receives processed images that crop and mask original images based on mask predictions $\{m_n(t)\}_{n=1}^N$ of BDFP and outputs the location-agnostic class prediction $\{p_n^a(t)\}_{n=1}^N$. For simplicity, we use a vision Transformer pre-trained on natural images as LACls in this work. We define the class token of the last layer as location-agnostic object query embedding e^a .

$$\mathcal{L}_{LACls} = \sum_{n=1}^N \mathbf{CE}(p_n^a, \tilde{c}_n). \quad (10)$$

Considering better trade-off between training costs and performance, we train this module only once for each fold offline. With the plug-and playable design, the trained module can be inserted into any instance segmentation architecture directly. For training this module offline, we use mask ground-truths instead of mask predictions and supervised by cross entropy loss \mathcal{L}_{LACls} as in Eq. (10). During inference, the module is cascaded directly after BDFP and makes classification based on mask segmentation predictions.

Algorithm 2 LACOSTE Train Algorithm

Input: Batchsize B , Batch Item (current frame $\mathcal{I}^L(t_i)$, stereo frame $\mathcal{I}^R(t_i)$, temporal frame $\mathcal{I}^L(t_i + \Delta t)$, temporal-stereo frame $\mathcal{I}^R(t_i + \Delta t)$), Pseudo Identity ID Label function \mathcal{F}_{id} .
Params: BDFP Φ_B , STSCls Φ_S , Initial Queries Q .

```

1: for each iteration do
2:   Frame Step
3:   for  $i \leftarrow 1$  to  $B$  do
4:     for  $j \leftarrow \text{in } \{t_i, t_i + \Delta t\}$  do
5:       if  $j = t_i + \Delta t$  then
6:          $Q = \{e_n^{b,\mathcal{L}}(t_i)\}_{n=1}^N$             $\triangleright$  Query Alignment
7:       else
8:          $Q = \{q_n\}_{n=1}^N$ 
9:       end if
10:       $\Phi_B(\mathcal{I}^L(j), \mathcal{I}^R(j)) \xrightarrow[\mathcal{L}^R]{Q} \bigcup \{(e_n^b(j), p_n^b(j), m_n(j))\}_{n=1}^N$ 
11:    end for                                 $\triangleright$  Label Pseudo Identity ID
12:     $\mathcal{F}_{id}(e_n^{b,\mathcal{L}/\mathcal{R}}(t_i/(t_i + \Delta t))) \rightarrow (i - 1) * N + n$ 
13:  end for
14:  Calculate  $\mathcal{L}_{baseline}$ 
Tracklet Step
15:  Filter out non-object queries            $\triangleright$  Identity Matching
16:  Mix multi-layers/sources/identities/categories queries
17:  Sample  $N_s$  augmented tracklets
18:  for  $n \leftarrow 1$  to  $N_s$  do
19:     $\Phi_S(s_n) \rightarrow (e_n^s, c_n^s)$ ,  $s_n$  means a tracklet
20:  end for
21:  Calculate  $\mathcal{L}_{STSCls}$ 
Optimize  $\Phi_B$ ,  $\Phi_S$ 
22: end for

```

4.5. Overall Training & Inference Pipeline.

In fact, LACOSTE can be trained in an end-to-end fashion. However, to reduce the training costs, we train the BDFP and STSCls jointly as Algorithm 2 and train LACls only once for each fold separately. In training stage, the formers are supervised with a combined loss as represented in Eq. (11) and the latter is optimized with \mathcal{L}_{LACls} .

$$\mathcal{L}_{total} = \mathcal{L}_{baseline} + \mathcal{L}_{STSCls}. \quad (11)$$

In inference stage, LACOSTE receives an 8-timestep (8 \times 2 frames) stereo clip centering at current frame $\mathcal{I}^L(t^*)$ and make end-to-end predictions as Algorithm 1. The final outputs of LACOSTE for current frame $\mathcal{I}^L(t^*)$ are composed of binary masks $\{m_n^L(t^*)\}_{n=1}^N$ and class predictions $\{p_n^{f,\mathcal{L}}(t^*)\}_{n=1}^N$.

5. Experiments

We experiment our LACOSTE on two public benchmark datasets of surgical videos, EndoVis2017 and EndoVis2018. Furthermore, dataset in other surgical domain, GraSP, is applied

Table 2. Performance of SOTA SIS methods on EV17 and EV18 instrument segmentation datasets. (BF-Bipolar Forceps, PF-Prograsp Forceps, LND-Large Needle Driver, VS/SI- Vessel Sealer/ Suction Instrument, GR/CA- Grasping Retractor/Clip Applier, MCS-Monopolar Curved Scissors, UP-Ultrasound Probe)

Method	Ch_IoU	ISI_IoU	Instrument Classes IOU						mc_IoU	
	BF	PF	LND	VS/SI	GR/CA	MCS	UP			
Dataset EV17										
TernausNet-11 (Shvets et al., 2018)	35.27	12.67	13.45	12.39	20.51	5.97	1.08	1.00	16.76	10.17
MF-TAPNET (Jin et al., 2019)	37.35	13.49	16.39	14.11	19.01	8.11	0.31	4.09	13.40	10.77
ISINET (González et al., 2020)	55.62	52.20	38.70	38.50	50.09	27.43	2.01	28.72	12.56	28.96
TraSeTR (Zhao et al., 2022)	60.40	65.20	45.20	56.70	55.8	38.90	11.40	31.30	18.20	36.79
S3Net (Baby et al., 2023)	72.54	71.99	75.08	54.32	61.84	35.50	27.47	43.23	28.38	46.55
MATIS (Frame) (Ayobi et al., 2023)	62.74	68.79	66.18	50.99	52.23	32.84	15.71	19.27	23.90	37.30
MATIS (Full) (Ayobi et al., 2023)	71.36	66.28	68.37	53.26	53.55	31.89	27.34	21.34	26.53	41.09
QPD (Dhanakshirur et al., 2023)	77.80	79.58	70.61	45.84	80.01	63.41	33.64	66.57	35.28	49.92
LACOSTE (S)	76.32	72.37	73.24	52.04	60.41	38.73	0.00	54.53	67.88	48.22
LACOSTE (B)	82.31	78.56	82.45	67.35	67.75	52.18	15.53	74.33	81.87	61.21
LACOSTE (L)	83.41	80.35	80.39	68.93	80.84	42.26	13.16	90.02	80.96	63.73
Dataset EV18										
TernausNet-11 (Shvets et al., 2018)	46.22	39.87	44.20	4.67	0.00	0.00	0.00	50.44	0.00	14.19
MF-TAPNET (Jin et al., 2019)	67.87	39.14	69.23	6.10	11.68	14.00	0.91	70.24	0.57	24.68
ISINET (González et al., 2020)	73.03	70.97	73.83	48.61	30.98	37.68	0.00	88.16	2.16	40.21
TraSeTR (Zhao et al., 2022)	76.20	-	76.30	53.30	46.50	40.60	13.90	86.30	17.50	47.77
S3Net (Baby et al., 2023)	75.81	74.02	77.22	50.87	19.83	50.59	0.00	92.12	7.44	42.58
MATIS (Frame) (Ayobi et al., 2023)	82.37	77.01	83.35	38.82	40.19	64.49	4.32	93.18	16.17	48.65
MATIS (Full) (Ayobi et al., 2023)	84.26	79.12	83.52	41.90	66.18	70.57	0.00	92.96	23.13	54.04
QPD (Dhanakshirur et al., 2023)	77.77	78.43	82.80	60.94	19.96	49.70	0.00	93.93	0.00	43.84
LACOSTE (S)	85.20	82.41	85.21	70.75	68.02	62.64	12.81	91.98	0.00	55.92
LACOSTE (B)	86.48	85.09	85.93	75.68	77.56	72.99	29.63	92.56	15.48	64.26
LACOSTE (L)	86.78	85.68	85.71	77.68	67.97	76.39	45.29	93.27	22.27	66.94

to validate the generality of method. Especially, we conduct comparison with state-of-the-art approaches, extensive ablation analysis on key components, and detailed visualization to validate the effectiveness of our approach.

5.1. Datasets & Implementation

EndoVis2017 (EV17). The EndoVis2017 dataset (Allan et al., 2019) comprises ten video sequences captured from the da-Vinci robotic surgical system, accompanied by **instance** annotations for six distinct robotic instruments and an ultrasound probe. In order to facilitate equitable comparisons, we adopt a four-fold cross-validation in common with previous methods from a total of 1,800 frames (8×225). The fold-wise split yields 1,350 and 450 frames for training and validation, respectively.

EndoVis2018 (EV18). The EndoVis2018 dataset (Allan et al., 2020) is collected from 2018 MICCAI Robotic Scene Segmentation Challenge. This dataset consists of 19 sequences, officially divided into 15 for training and 4 for testing. Each training sequence contains 149 frames recorded on a da Vinci X or Xi system during porcine training procedure. Each frame has a high resolution of 1280×1024 . We use pre-defined training and validation splits from (Shvets et al., 2018) and annotate **instances** by ourselves for experiments.

GraSP (GRASP). The GraSP dataset (Ayobi Mendoza, 2023) is a new curated benchmark that models surgical scene understanding. This dataset contains 13 sequences, officially divided

into 8 for training and 5 for testing. This dataset provides multi-granularity including short-term segmentation and long-term recognition annotations. Each frame has a high resolution of 800×1280 . It's noteworthy that GraSP provides monocular consecutive frames but only pixel-wise segmentation annotation for 3449 sparse frames. We use pre-defined training and validation splits from (Ayobi Mendoza, 2023).

Metrics. For all datasets, we evaluate the performance on the Challenge IoU (Ch_IoU) metric as proposed in the EndoVis2017 challenge and ISINET IoU (ISI_IoU) and mean class IoU (mc_IoU) metrics proposed in (González et al., 2020), to facilitate comparison. The formulas of metrics are represented in Eq. (12), wherein P/G mean segmentation predictions/ground truths, C/\tilde{C}_i mean all classes/ground truth classes of current frame and K represents number of frames.

$$\begin{aligned}
 \text{Ch_IoU} &= \frac{1}{K} \sum_{i=1}^K \left(\frac{1}{\tilde{C}_i} \sum_{c=1}^{\tilde{C}_i} \frac{P_{i,c} \cap G_{i,c}}{P_{i,c} \cup G_{i,c}} \right) \\
 \text{ISI_IoU} &= \frac{1}{K} \sum_{i=1}^K \left(\frac{1}{C} \sum_{c=1}^C \frac{P_{i,c} \cap G_{i,c}}{P_{i,c} \cup G_{i,c}} \right) \\
 \text{mcIoU} &= \frac{1}{C} \sum_{c=1}^C \left(\frac{1}{K} \sum_{i=1}^K \frac{P_{i,c} \cap G_{i,c}}{P_{i,c} \cup G_{i,c}} \right)
 \end{aligned} \tag{12}$$

Implementation Details. Our framework is implemented

based on Mask2Former and initialized by pretrained parameters with coco instance segmentation. All frames are resized into a range of (256, 1024) and crop 640×512 (640×400 for GRASP) images randomly. The augmentation is consistent across the stereo, temporal, and current frames. We deploy the AdamW optimizer with a poly learning rate scheduler and use a base learning rate of $1e-4$. Batch size is set to 4 or 8 based on GPU size and the clip length is empirically set to 8. We select top five instances for each frame to merge semantic segmentation results like other methods e.g. (Baby et al., 2023; Dhanakshirur et al., 2023; Ayobi et al., 2023).

5.2. Main Results

EndoVis 2017 & 2018. We compare our LACOSTE with state-of-the-art approaches including not only single frame methods, S3Net and QPD, but also temporal methods, MATIS. For fair comparison, we validate our approach based on Mask2Former with different backbones. For most experiments in this work, We implement our method based on SwinBase backbone. To compare with MATIS, we implement a parameters-equivalent one with the same SwinSmall backbone. QPD is implemented with MaskDino (Li et al., 2023), which is designed with a SwinLarge backbone and 300 queries. We also present a heavy-weight model with a SwinLarge backbone in this paper. For simplicity, we symbol SwinBase, SwinSmall and SwinLarge as **B**, **S** and **L** in the following parts. Results of different methods are presented in Table 2. We export the best results of comparison methods reported in their papers. For EV17, LACOSTE(**B**) and LACOSTE(**L**) outperforms all other methods while LACOSTE(**S**) is inferior to QPD because of less parameters. LACOSTE(**L**) improves over QPD by **7%** Ch.IoU, **1%** ISI.IoU, and **28%** mIoU showing that temporal-stereo information improves the results by a considerable margin. Even for other temporal consistency methods, LACOSTE(**S**) outperforms MATIS by an improvement of **7%** Ch.IoU, **9%** ISI.IoU and **17%** mIoU while LACOSTE(**L**) improves **17%** Ch.IoU, **21%** ISI.IoU and **55%** mIoU respectively. For EV18, LACOSTE is superior to single frame methods obviously. LACOSTE(**L**) improves over QPD by **12%** Ch.IoU, **9%** ISI.IoU, and **53%** mIoU. Moreover, LACOSTE(**S**) precedes MATIS slightly with **1%** Ch.IoU, **4%** ISI.IoU, and **3%** mIoU while LACOSTE(**L**) improves **3%**, **8%**, and **24%**, respectively. As noted above, temporal information is more effective for EV18 and enhancing inter-instruments discrepancy is more important for EV17. The performance improvement between LACOSTE(**B**) and LACOSTE(**S**) is more obvious than that changing the backbone from SwinBase to SwinLarge. For better trade-off between training costs and performance, we validate the following experiments and analysis based on LACOSTE(**B**).

GraSP. We compare our LACOSTE with TAPIS (Ayobi Mendoza, 2023) which is a multi-task method for surgical scene understanding and other state-of-the-art approaches reported in their paper. Evaluations are implemented not only in semantic segmentation but also in instance segmentation. In particular, Ch.IoU, ISI.IoU and mIoU are selected for semantic performance while AP50_{box} and AP50_{segm} are used for instance performance. Results of different methods are presented

in Table 3. Observe that LACOSTE(**L**) attains the best overall results of 80.07 mIoU and 84.81 ISI.IoU. In the task of instance segmentation, as measured by the AP50_{segm} metric, LACOSTE (**B**) demonstrates superior performance compared to all other evaluated methods, while LACOSTE (**L**) achieves the second highest performance. TAPIS (Frame) and TAPIS (Full) respectively outperform LACOSTE in AP50_{box} and Ch.IoU. This superior performance is likely attributable to the multi-task architecture and the incorporation of additional annotations, such as those for detection and phase recognition. But promisingly, LACOSTE achieves peak or second segmentation performance across most evaluation metrics. This result suggests that our method is robust and generality to various surgical domain. When comparing the improvement of LACOSTE with that of EV17 and EV18, the enhancement may be constrained by limited binary mask segmentation for GRASP, which is not the primary design focus of this paper.

5.3. Ablation Study

We conduct ablation experiments to validate the effectiveness of different key components in the proposed method and obtain seven configurations:

- (a) **Baseline:** We train the pure Mask2former network as the baseline;
- (b) **Baseline (DFP):** We train the baseline Mas2former with DFP;
- (c) **Baseline (DFP, T):** We train STSCls with augmented tracklets by mixing object queries across only temporal dimension;
- (d) **Baseline (DFP, S):** We train STSCls with augmented tracklets by mixing object queries across only stereo dimension;
- (e) **Baseline (DFP, ST):** We train STSCls with augmented tracklets by mixing object queries across both temporal and stereo dimensions;
- (f) **Baseline (DFP, ST, LACls):** We apply a LACls without fine-tuning after (e);
- (g) **Baseline (DFP, ST, LACls):** We fine-tune a LACls after (e) for some iterations;

Effectiveness of Key Components. The results on EV17 and EV18 are presented in Table 4. We observe that our baseline based on SwinBase backbone obtains reasonable results with Ch.IoU and ISI.IoU over 70 on all tasks of both datasets. Purely introducing DFP module on stereo dimension, (b) achieves better results by **4%** Ch.IoU, **3%** ISI.IoU, **8%** mIoU for EV17 and **2%** Ch.IoU, **3%** ISI.IoU, **7%** mIoU for EV18. Incorporating temporal-stereo consistency cues by STSCls, (c) (d) (e) further improves the segmentation performance in all evaluation metrics of both datasets. For different augmented tracklets configure settings, we observe that (e) is superior to the other two on most metrics especially mIoU. We compare (e) with (b) to evaluate the effectiveness of STSCls intuitively. Ch.IoU and ISI.IoU on EV17 are increased respectively **3.55**, and **4.39**. The same trends rising **1.69** Ch.IoU and **1.5** ISI.IoU can also be observed on EV18. Adding our LACls without any fine-tuning operations, our full model continues boosting the results with **0.4** Ch.IoU and **0.4~1** ISI.IoU gain,

Table 3. Performance of SOTA SIS methods on GRASP. Ch_IoU, ISI_IoU and mcIoU are the same as above for semantic segmentation.

Methods	Instance Segmentation		Semantic Segmentation		
	AP50 _{box}	AP50 _{segm}	Ch_IoU	ISI_IoU	mcIoU
Dataset GRASP					
TernausNet-11 (Shvets et al., 2018)	-	-	41.74	24.46	16.87
MF-TAPNet (Jin et al., 2019)	-	-	66.63	29.23	24.98
ISINet (González et al., 2020)	79.85	78.29	78.44	70.85	56.67
QPD (Dhanakshirur et al., 2023)	88.46	87.39	83.89	82.56	74.36
TAPIS (Frame) (Ayobi Mendoza, 2023)	92.65	91.71	86.91	83.92	77.59
TAPIS (Full) (Ayobi Mendoza, 2023)	91.72	90.34	87.05	84.45	78.82
LACOSTE (S)	89.69	90.83	86.14	84.04	78.23
LACOSTE (B)	91.80	92.39	86.77	83.95	79.44
LACOSTE (L)	90.72	92.15	86.37	84.81	80.07

Table 4. Performance of key components on EV17 and EV18. ✓ in LACls column means fine-tuning LACls.

Key Components	Ch_IoU	ISI_IoU	Instrument Classes IOU						mcIoU	
			BF	PF	LND	VS/SI	GR/CA	MCS	UP	
Dataset EV17										
DFP	75.12	71.68	60.42	62.97	60.88	36.29	3.14	30.22	46.00	44.48
✓	78.34	74.13	74.19	64.57	55.17	38.01	10.19	35.22	49.24	47.88
✓	T	81.21	78.02	74.72	68.63	90.03	53.49	27.52	41.49	52.62
✓	S	81.12	78.19	74.65	62.13	66.80	37.66	14.26	77.51	53.64
✓	ST	81.89	78.52	82.77	67.86	67.90	51.70	15.40	73.90	81.87
✓	ST	✓	82.31	78.56	82.45	67.35	67.75	52.18	15.53	74.33
✓	ST	✓	82.90	79.05	82.89	67.24	68.02	52.71	17.53	74.59
Dataset EV18										
✓	82.93	80.54	85.23	69.42	45.37	56.36	0.00	91.99	0.00	49.77
✓	84.33	82.92	85.42	74.01	64.12	53.39	0.00	92.74	3.38	53.29
✓	T	85.72	84.08	86.37	71.77	67.26	76.20	6.71	92.42	21.99
✓	S	85.90	83.99	85.90	72.28	72.36	71.51	0.00	93.18	0.00
✓	ST	86.02	84.42	85.94	75.99	79.25	70.37	2.53	92.78	7.44
✓	ST	✓	86.48	85.09	85.93	75.68	77.56	72.99	29.63	92.56
✓	ST	✓	86.66	85.35	85.89	75.37	75.94	73.26	53.58	92.77
12.28										
6.70										

peaking at **82.31** Ch_IoU, **78.56** ISI_IoU on EV17 and **86.48** Ch_IoU **85.09** ISI_IoU on EV18. The architecture achieves **82.90** Ch_IoU, **79.05** ISI_IoU, **61.76** mcIoU for EV17 and **86.66** Ch_IoU, **85.35** ISI_IoU, **67.01** mcIoU for EV18 with some iterations fine-tuning. To reduce training costs, we report our methods based on SwinSmall, SwinBase and SwinLarge backbone in last subsection without any fine-tuning.

Performance of Ensemble Items. We list the performance of each item in final ensemble results as Table 5. LACOSTE (F), LACOSTE (S), LACOSTE (A) mean the results of the Frame, Tracklet, and L-Agnostic step, respectively. The effectiveness of ensemble mechanism can be validated on both datasets. Among all items, STSCls of Tracklet step exerts the most significant influence on ISI_IoU and mcIoU while LACls of L-Agnostic step demonstrates superior performance in Ch_IoU. In the context of instrument classes IOU, items exhibit mutual complementarity across various instrument types.

Pseudo Stereo Generation. To validate the effectiveness of pseudo stereo generation mechanism for only monocular dataset, we experiment LACOSTE respectively with real right images and generated pseudo right images for both datasets. The results are presented in Table 6, where LACOSTE(P)

means the experiments with pseudo generation. We observe that the results decrease **0.21** in Ch_IoU, **0.56** in ISI_IoU, and **9** in mcIoU but outperform the baseline (a) on EV17. The results on EV18 decrease **0.91** in Ch_IoU, **0.89** in ISI_IoU, and **9** in mcIoU. The decreasing performance is within an acceptable range. The slight misclassification on non-existent classes of validation dataset makes the mcIoU metric decrease obviously. The pseudo stereo generation mechanism can complement monocular dataset to some extent.

Non-object Masking. For surgical domain, the same instance can move out of view through a stereo clip, where object query fails to match with any instance in some frames. As mentioned above, object query not corresponding to any instance is named as *non-object query*, which can be determined based on BDFFP classification. We also investigate the influence of masking out non-objects queries within a self-attention operation of STSCls in inference stage. The results are presented in Table 7, where LACOSTE(M) means the experiments with masking operation. We find that masking non-object queries is superior for EV18 but inferior for EV17. The rationale behind this may be that EV18 contains more move-out-of-view situations than EV17 dataset. Masking operation decreases the influence of noise in-

Table 5. Performance of ensemble items of LACOSTE on EV17 & EV18.

Method	Ch_	ISI_	Instrument Classes IOU						mc	
	IoU	IoU	BF	PF	LND	VS/ SI	GR/ CA	MCS	UP	IoU
Dataset EV17										
LACOSTE (F)	81.39	76.18	80.19	60.69	63.80	38.08	10.93	37.05	40.62	49.68
LACOSTE (S)	81.60	78.25	81.64	67.97	67.60	51.69	16.15	48.70	81.62	59.05
LACOSTE (A)	81.76	76.43	79.13	59.74	62.74	39.14	11.68	52.76	40.52	49.38
LACOSTE	82.31	78.56	82.45	67.35	67.75	52.18	15.53	74.33	81.87	61.21
Dataset EV18										
LACOSTE (F)	85.34	83.73	85.58	74.63	72.15	64.94	13.68	91.75	5.62	58.34
LACOSTE (S)	85.85	84.36	86.09	76.42	77.39	67.12	8.03	92.77	0	58.26
LACOSTE (A)	86.04	84.59	85.87	75.00	74.05	71.58	17.89	92.36	17.40	62.02
LACOSTE	86.48	85.09	85.93	75.68	77.56	72.99	29.63	92.56	15.48	64.26

Table 6. Performance of pseudo stereo mechanism on EV17 & EV18.

Method	Ch_	ISI_	Instrument Classes IOU						mc	
	IoU	IoU	BF	PF	LND	VS/ SI	GR/ CA	MCS	UP	IoU
Dataset EV17										
LACOSTE	82.31	78.56	82.45	67.35	67.75	52.18	15.53	74.33	81.87	61.21
LACOSTE (P)	82.10	78.00	78.36	67.24	65.75	39.43	27.97	44.08	75.95	52.19
Dataset EV18										
LACOSTE	86.48	85.09	85.93	75.68	77.56	72.99	29.63	92.56	15.48	64.26
LACOSTE (P)	85.57	84.20	86.46	77.43	73.70	54.09	2.66	93.69	0.00	55.43

Table 7. Influence of non-object masking mechanism on EV17 and EV18.

Method	Ch_	ISI_	Instrument Classes IOU						mc	
	IoU	IoU	BF	PF	LND	VS/ SI	GR/ CA	MCS	UP	IoU
Dataset EV17										
LACOSTE	82.31	78.56	82.45	67.35	67.75	52.18	15.53	74.33	81.87	61.21
LACOSTE (M)	81.53	77.57	81.03	61.07	63.57	40.28	14.26	78.52	40.83	52.66
Dataset EV18										
LACOSTE	86.09	84.50	86.10	76.00	78.40	71.05	7.51	92.56	15.48	58.80
LACOSTE (M)	86.48	85.09	85.93	75.68	77.56	72.99	29.63	92.56	15.48	64.26

formation.

optimization methods (e.g., TensorRT) can further reduce the latency of model.

Other Metrics. We also provide some other metrics to evaluate our methods from different perspectives. In particular, we select Dice similarity coefficient (DSC)/F1 score, mean class Dice (mcD), Hausdorff distance (HD) and average surface distance (ASD). The former two metrics are commonly used to evaluate the effectiveness of segmentation methods. HD and ASD are sensitive to the boundaries of segments, which represent segmentation completeness in some certain. The results are shown in Table 9, where baseline means the results of original Mask2Former. For all benchmarks, LACOSTE(L) demonstrates superior performance in both DSC and mcD metrics. In the assessment of segmentation completeness, LACOSTE(L) demonstrates inferior performance compared to LACOSTE(B) as indicated by higher values in HD and ASD metrics for EV17 and EV18 while LACOSTE(L) exhibits superiority in GRASP.

5.4. Qualitative Analysis

Segmentation Results. Figure 5 illustrates the qualitative segmentation results. We show the comparative results of a sin-

Table 8. Inference time for proposed components of LACOSTE on EV17.

Key Components	Inference		Ch_	ISI_	mc		
	DFP	STSCls	LACls	Time (s)	IoU	IoU	IoU
				0.219	75.12	71.68	44.48
✓				0.323	78.34	74.13	47.88
✓	ST			0.343	81.89	78.52	61.26
✓	ST	✓		0.371	82.31	78.56	61.21

Inference Time. We analyze the inference time of each proposed component as Table 8. For improving model efficiency and reducing inference time, we introduce a memory bank to record intermediate results including features, embeddings and predictions which can be reused across different clips. Furthermore, we also record corresponding valid object queries indices which can reduce the computations of LACls. In comparison with baseline model, LACOSTE requires additional computation for temporal and stereo contexts, but the performance gain over additional latency is substantial. We expect that inference

Table 9. More metrics of our methods in three surgical instrument datasets. DSC(\uparrow) and mcD(\uparrow) can show the segmentation accuracy. HD(\downarrow) and ASD(\downarrow) show the segmentation completeness.

Method	EV17				EV18				GRASP			
	DSC(\uparrow)	mcD(\uparrow)	HD(\downarrow)	ASD(\downarrow)	DSC(\uparrow)	mcD(\uparrow)	HD(\downarrow)	ASD(\downarrow)	DSC(\uparrow)	mcD(\uparrow)	HD(\downarrow)	ASD(\downarrow)
Baseline	75.49	47.15	163.60	39.93	84.38	52.32	108.79	13.90	84.85	76.97	106.04	13.57
LACOSTE(S)	76.46	51.11	134.76	19.68	86.33	59.02	142.04	18.62	88.06	82.68	95.71	18.62
LACOSTE(B)	82.22	64.20	90.26	14.89	88.94	64.26	103.90	12.82	87.97	83.89	95.80	10.21
LACOSTE(L)	84.11	66.91	94.54	12.60	89.68	70.90	122.45	15.80	88.72	84.39	94.35	9.89

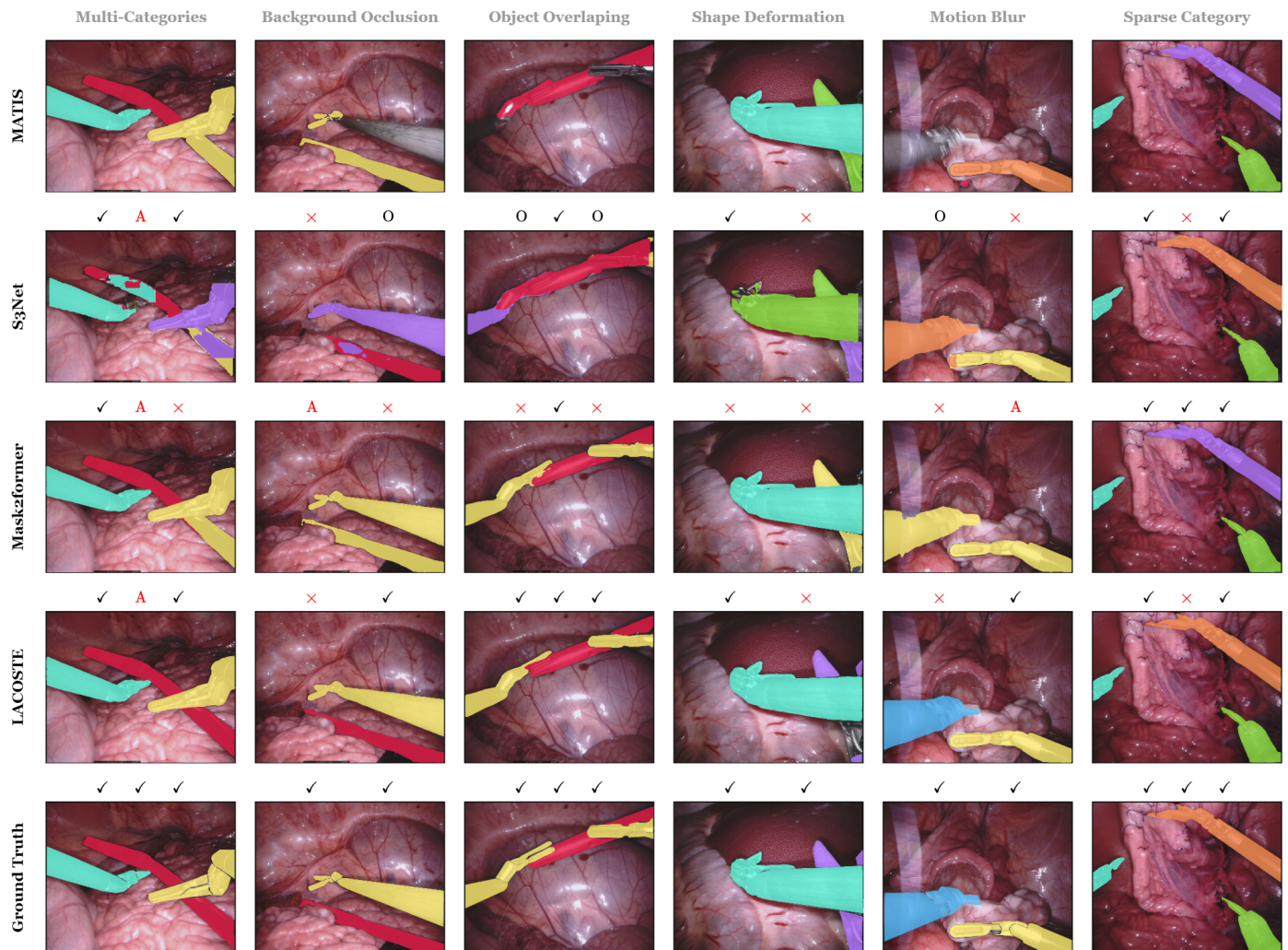


Fig. 5. Qualitative analysis for SIS results: different symbols are used to show the results; \checkmark represents the instance labeled correctly, \times shows the misclassified instance, and 'O' represents missed instance. The letter **A** is employed to denote instances characterized by ambiguity, wherein the selection of the appropriate instrument class is rendered uncertain. This ambiguity may arise from factors such as over-segmentation or the presence of multiple instances of instrument classes within the same spatial region.

gle frame approach named S3Net, a typical temporal consistency approach named MATIS, our baseline, and our proposed approach. The segmentation results are distributed across different situations including multi-categories, background occlusion, object overlapping, shape deformation, motion blur, and sparse category. We show better segmentation in most situations. LACOSTE also focuses on perceiving the temporal context and performs well in classifying motion blur, background occlusion and shape deformation circumstances.

Query Embedding Space Analysis. We make t-SNE analysis of frame object queries embeddings e^b from BDFP (FOE), tracklet object queries embeddings e^s from STSCls (TOE) and location-agnostic object queries embeddings e^a from LACls (LAOE) as shown in Figure 6. For both FOE and TOE, query embedding spaces are partitioned into discriminative clusters and the latter exhibits a more compact structure. Additionally, except the Large Needle Driver (LND) and Prograsp Forceps (PF), the queries embeddings are distributed around one clus-

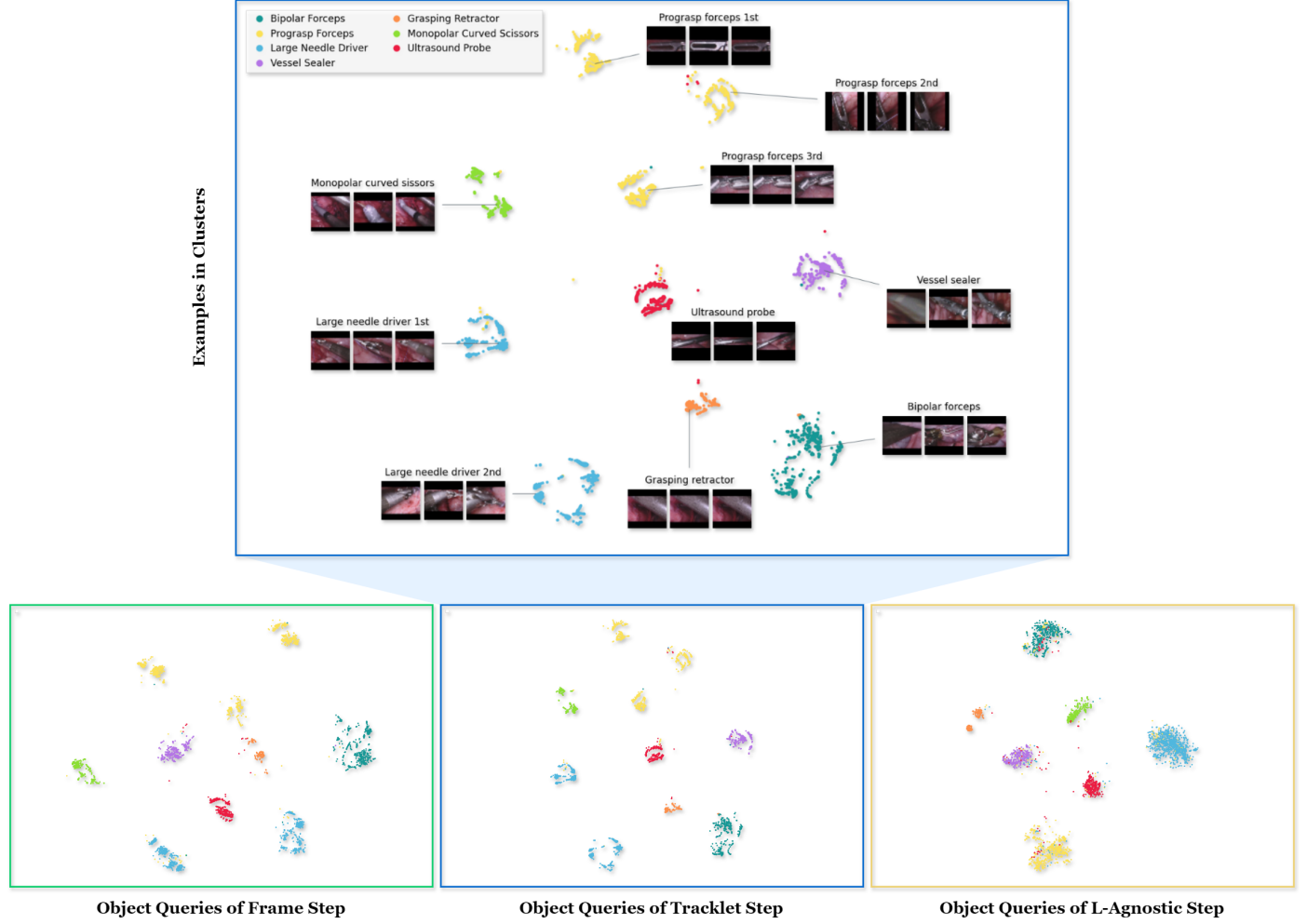


Fig. 6. T-SNE analysis of query embedding space from each step. Instance examples of each cluster in tracklet object queries space are also visualized.

ter. In Figure 6, we visualize some instance examples for every cluster in TOE. As illustrated in ‘Large Needle Driver 1st’ and ‘Large Needle Driver 2nd’ instance examples, the location and orientation of the category have a significant change which arises the cluster deviation. Furthermore, rather than ‘Large Needle Driver 2nd’, the cluster of ‘Large Needle Driver 1st’ is closer to ‘Monopolar Curved Scissors’. The location bias may have a negative influence in semantic classification. After inducing LACIs, the multi-clusters of LND and PF in LAOE space can collapse into only one. It is worth noting that the embedding projection points of TOE space are fewer than the other two because the examples belonging to one clip project into the same location.

Query Alignment Analysis. As mentioned in 4.3, it is assumed that object queries within a stereo clip, indexed by the same object query index, are assigned with the same identity ID after query alignment operation and the application of identity alignment loss constraints. This assumption serves to streamline the generation of tracklets without the need for video annotations. To validate the effectiveness of these mechanisms in preserving identity consistency, we present the graphical relationship between query indexes and identity IDs through a stereo clip as illustrated in Figure 7. Distinct rows are indicative of different examples, whereas columns represent dif-

ferent methodologies. For each circular chart, the eight rings from outermost to innermost correspond to eight continuous frames, with 100 query indexes distributed along the counter-clockwise direction of each ring. The items highlighted in color indicate object queries that correspond to specific instances, whereas the gray items represent non-object queries. The corresponding color is set based on the category of matched instance. If **the same instance is aligned with same query index across different frames**, these mechanisms can fulfill the assumption. For comparison, we visualize baseline, our proposed method with only identity alignment loss constraints and full LACOSTE. The first two columns of Figure 7 show that only introducing the identity alignment loss can enhance the identity consistency relative to baseline. The query alignment mechanism deepens the above advantage as illustrated in the last two columns. However, it is worth noting that two mechanisms of LACOSTE are more suitable for short clips rather long videos. For fast motion and severe deformation circumstances, the methods are more inclined to find another new query index aligned with identity like tracking methods. The examples of Figure 7 keep the same with those of Figure 8 and Figure 9.

Embedding Similarity Analysis. To illustrate the identity consistency encoded in object queries more effectively, we visualize query embedding similarities across both temporal and

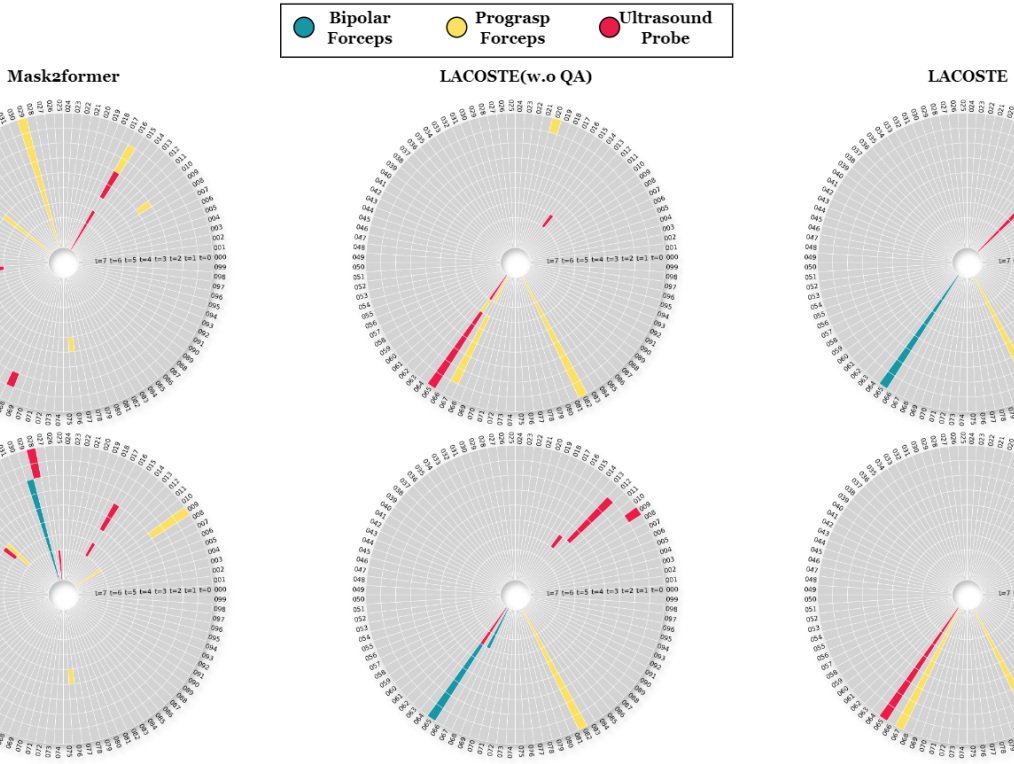


Fig. 7. Comparison of Query Alignment Situations. The rings from outermost to innermost represent eight temporal frames. The counterclockwise direction of each ring represents 100 query indexes. LACOSTE(w.o QA) means our proposed method with only identity alignment loss constrains while LACOSTE means the full model.



Fig. 8. Quality Analysis of identity consistency in one stereo clip from embedding similarity perspectives. Every ring of circular chart represents the similarities between one valid object query of reference frame and 100 object queries of target frame. Valid object queries are ascertained by Hungarian Matching. The ring color is set based on the category of valid object query.

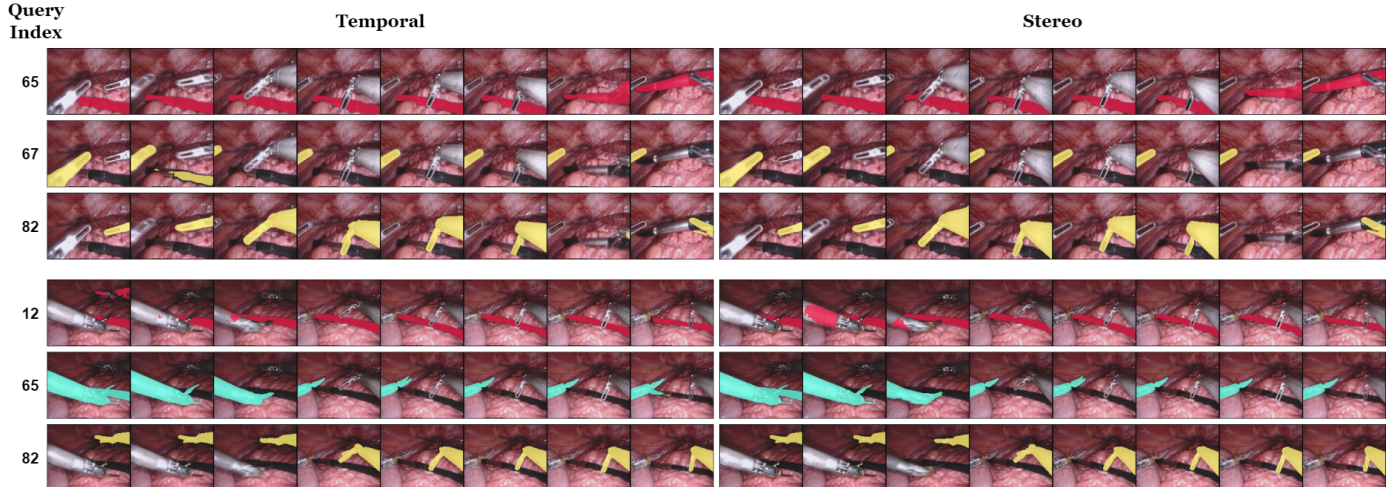


Fig. 9. Quality Analysis of identity consistency in one stereo clip from query segmentation perspectives.

stereo frames as shown in Figure 8. Rows denote examples while columns respectively represent interval-3, inter-1 temporal frames and stereo frame. For every ring of circular chart, a valid object query of current frame is analyzed for similarities with all 100 object queries from temporal or stereo frame. If the similarity value between object queries with the same index is higher, the method achieves greater identity consistency. In particular, for the first row example, the valid object queries of the current frame are the 12th, 65th, and 82nd as indicated in the LACOSTE column of Figure 7. As for query 65th ring, the peak similarities are concentrated at the 65th bar in all charts of first row, thereby preserving identity consistency. Analogous situations can be observed in other instances. We also visualize the segmentation results for each valid object query through a stereo clip to present the identity consistency explicitly as shown in Figure 9.

Table 10. Evaluation on temporal consistency of segmentation results.

Method	EV18			
	Ch_IoU	\mathcal{J}	\mathcal{F}	$\mathcal{J} \& \mathcal{F}$
XMEM	70.2	72.3	72.0	72.2
XMEM(F)	72.6	73.1	73.6	73.4
SAM2	82.6	81.4	81.5	81.4
SurgSAM-2	84.4	84.3	84.0	84.1
SurgSAM-2(P)	84.1	84.2	83.8	84.0
LACOSTE(S)	85.2	85.8	85.3	85.5

Temporal Consistency of Segmentation Results. We further analyze our temporal consistency of segmentation results together with some video object segmentation (VOS) methods including SAM2 (Ravi et al., 2024; Shen et al., 2024) and SurgSAM-2 (Liu et al., 2024) which is based on SAM2 and fine-tuned with EV18. We also supplement fine-tuned results of XMEM (Cheng and Schwing, 2022) with the same dataset, represented as XMEM(F). Actually, ours and VOS paradigms are inherently tailored for distinct tasks with different challenges. It is important to clarify that our intention is not to assert a superior temporal consistency compared to VOS methods. Instead, we aim to offer researchers potential insights and **feasible**

alternatives for establishing temporal correlations in scenarios where video-level annotations are unavailable. The temporal consistency of segmentation results, which is not the primary focus or contribution of this paper, is an inherited outcome by mitigating misclassification and improving segmentation effectiveness. Particularly, VOS methods receive the annotated first frame for each object of the video sequence and propagate them through time dimension. For the LACOSTE model, we maintain the original inference process without utilizing any annotation. We present several VOS metrics, including Jaccard index \mathcal{J} , contour accuracy \mathcal{F} , and their average $\mathcal{J} \& \mathcal{F}$, together with semantic segmentation metric Ch_IoU in Table 10. We use category IDs as object IDs in these experiments. For all metrics, LACOSTE achieves comparable or favorable results with the other methods. In fact, our method does not require any annotations during inference process while the competing methods require so. Additionally, we substitute the annotations of reference frames with our predictions for SurgSAM-2 to validate the cooperative potential, denoted as SurgSAM-2(P). Our approach can deliver semantic prompts for category-agnostic SAM2-based VOS methods when reference annotations are unavailable.

6. Conclusion

In this study, we systematically explore temporal information and stereo cue in surgical instrument segmentation tasks. LACOSTE extends common query-based segmentation methods with proposed disparity-guided feature propagation module, stereo-temporal set classifier and location-agnostic classifier to mitigate surgical domain challenges. Exhaustive experiments have been conducted on the benchmark robot-assisted surgery datasets. Our method generalizes well on all benchmarks and achieves comparable or favorable results with previous state-of-the-art approaches. We conclude that introducing temporal and stereo information improves the results for applications involving complicated classification in different circumstances. The proposed framework can be helpful to downstream applications that depend on tool identification and segmentation. We hope

that our analysis and the innovations to mitigate the challenges specific to surgical instruments will spark similar interests in introducing specific information and attributes in other domains.

References

Allan, M., Kondo, S., Bodenstedt, S., Leger, S., Kadkhodamohammadi, R., Luengo, I., Fuentes, F., Flouty, E., Mohammed, A., Pedersen, M., et al., 2020. 2018 robotic scene segmentation challenge. arXiv preprint arXiv:2001.11190 .

Allan, M., Shvets, A., Kurmann, T., Zhang, Z., Duggal, R., Su, Y.H., Rieke, N., Laina, I., Kalavakonda, N., Bodenstedt, S., et al., 2019. 2017 robotic instrument segmentation challenge. arXiv preprint arXiv:1902.06426 .

Ayobi, N., Pérez-Rondón, A., Rodríguez, S., Arbeláez, P., 2023. Matis: Masked-attention transformers for surgical instrument segmentation. arXiv preprint arXiv:2303.09514 .

Ayobi Mendoza, N., 2023. Towards pixel-wise surgical instrument recognition with transformers .

Baby, B., Thapar, D., Chasmai, M., Banerjee, T., Dargan, K., Suri, A., Banerjee, S., Arora, C., 2023. From forks to forceps: A new framework for instance segmentation of surgical instruments, in: Proceedings of the IEEE/CVF Winter Conference on Applications of Computer Vision, pp. 6191–6201.

Bertasius, G., Torresani, L., 2020. Classifying, segmenting, and tracking object instances in video with mask propagation, in: Proceedings of the IEEE/CVF Conference on Computer Vision and Pattern Recognition, pp. 9739–9748.

Bouget, D., Allan, M., Stoyanov, D., Jannin, P., 2017. Vision-based and markerless surgical tool detection and tracking: a review of the literature. Medical image analysis 35, 633–654.

Cheng, B., Schwing, A., Kirillov, A., 2021. Per-pixel classification is not all you need for semantic segmentation. Advances in Neural Information Processing Systems 34, 17864–17875.

Cheng, H.K., Schwing, A.G., 2022. Xmem: Long-term video object segmentation with an atkinson-shiffrin memory model, in: European Conference on Computer Vision, Springer. pp. 640–658.

Curtis, N., Foster, J., Miskovic, D., Brown, C., Hewett, P., Abbott, S., Hanna, G., Stevenson, A., Francis, N., 2020. Association of surgical skill assessment with clinical outcomes in cancer surgery. *jama surg.*

Dhanakshirur, R.R., Shastry, K.A., Borgavi, K., Suri, A., Kalra, P.K., Arora, C., 2023. Learnable query initialization for surgical instrument instance segmentation, in: International Conference on Medical Image Computing and Computer-Assisted Intervention, Springer. pp. 728–738.

Ding, H., Wu, J.Y., Li, Z., Unberath, M., 2023. Rethinking causality-driven robot tool segmentation with temporal constraints. International Journal of Computer Assisted Radiology and Surgery 18, 1009–1016.

Dosovitskiy, A., Beyer, L., Kolesnikov, A., Weissenborn, D., Zhai, X., Unterthiner, T., Dehghani, M., Minderer, M., Heigold, G., Gelly, S., et al., 2020. An image is worth 16x16 words: Transformers for image recognition at scale. arXiv 2020. arXiv preprint arXiv:2010.11929 .

Du, X., Allan, M., Bodenstedt, S., Maier-Hein, L., Speidel, S., Dore, A., Stoyanov, D., 2019. Patch-based adaptive weighting with segmentation and scale (pawss) for visual tracking in surgical video. Medical image analysis 57, 120–135.

González, C., Bravo-Sánchez, L., Arbelaez, P., 2020. Isinet: an instance-based approach for surgical instrument segmentation, in: MICCAI, Springer. pp. 595–605.

Hasan, S., Linte, C.A., 2019. U-netplus: a modified encoder-decoder u-net architecture for semantic and instance segmentation of surgical instrument. arXiv preprint arXiv:1902.08994 .

He, K., Gkioxari, G., Dollár, P., Girshick, R., 2017. Mask r-cnn, in: Proceedings of the IEEE international conference on computer vision, pp. 2961–2969.

Hein, J., Seibold, M., Bogo, F., Farshad, M., Pollefeys, M., Fürnstahl, P., Navab, N., 2021. Towards markerless surgical tool and hand pose estimation. International journal of computer assisted radiology and surgery 16, 799–808.

Hwang, S., Heo, M., Oh, S.W., Kim, S.J., 2021. Video instance segmentation using inter-frame communication transformers. Advances in Neural Information Processing Systems 34, 13352–13363.

Hwang, S., Heo, M., Oh, S.W., Kim, S.J., 2022. Cannot see the forest for the trees: Aggregating multiple viewpoints to better classify objects in videos, in: Proceedings of the IEEE/CVF Conference on Computer Vision and Pattern Recognition, pp. 17052–17061.

Islam, M., Li, Y., Ren, H., 2019. Learning where to look while tracking instruments in robot-assisted surgery, in: International Conference on Medical Image Computing and Computer-Assisted Intervention, Springer. pp. 412–420.

Jin, Y., Cheng, K., Dou, Q., Heng, P.A., 2019. Incorporating temporal prior from motion flow for instrument segmentation in minimally invasive surgery video, in: Medical Image Computing and Computer Assisted Intervention–MICCAI 2019: 22nd International Conference, Shenzhen, China, October 13–17, 2019, Proceedings, Part V 22, Springer. pp. 440–448.

Jin, Y., Yu, Y., Chen, C., Zhao, Z., Heng, P.A., Stoyanov, D., 2022. Exploring intra-and inter-video relation for surgical semantic scene segmentation. IEEE Transactions on Medical Imaging 41, 2991–3002.

Ke, L., Li, X., Danelljan, M., Tai, Y.W., Tang, C.K., Yu, F., 2021. Prototypical cross-attention networks for multiple object tracking and segmentation. Advances in Neural Information Processing Systems 34, 1192–1203.

Li, F., Zhang, H., Xu, H., Liu, S., Zhang, L., Ni, L.M., Shum, H.Y., 2023. Mask dino: Towards a unified transformer-based framework for object detection and segmentation, in: Proceedings of the IEEE/CVF Conference on Computer Vision and Pattern Recognition, pp. 3041–3050.

Liu, D., Li, Q., Jiang, T., Wang, Y., Miao, R., Shan, F., Li, Z., 2021. Towards unified surgical skill assessment, in: Proceedings of the IEEE/CVF Conference on Computer Vision and Pattern Recognition, pp. 9522–9531.

Liu, H., Zhang, E., Wu, J., Hong, M., Jin, Y., 2024. Surgical sam 2: Real-time segment anything in surgical video by efficient frame pruning. arXiv preprint arXiv:2408.07931 .

Liu, Z., Hu, H., Lin, Y., Yao, Z., Xie, Z., Wei, Y., Ning, J., Cao, Y., Zhang, Z., Dong, L., Wei, F., Guo, B., 2022. Swin transformer v2: Scaling up capacity and resolution, in: CVPR.

Loftus, T.J., Tighe, P.J., Filiberto, A.C., Efron, P.A., Brakenridge, S.C., Mohr, A.M., Rashidi, P., Upchurch, G.R., Bihorac, A., 2020. Artificial intelligence and surgical decision-making. *JAMA surgery* 155, 148–158.

Maier-Hein, L., Eisenmann, M., Sarikaya, D., März, K., Collins, T., Malpani, A., Fallert, J., Feussner, H., Giannarou, S., Mascagni, P., et al., 2022. Surgical data science—from concepts toward clinical translation. *Medical image analysis* 76, 102306.

Maier-Hein, L., Vedula, S.S., Speidel, S., Navab, N., Kikinis, R., Park, A., Eisenmann, M., Feussner, H., Forestier, G., Giannarou, S., et al., 2017. Surgical data science for next-generation interventions. *Nature Biomedical Engineering* 1, 691–696.

Mohammed, A., Yıldırım, S., Farup, I., Pedersen, M., Hovde, Ø., 2019. Stremoscennet: surgical stereo robotic scene segmentation, in: Medical imaging 2019: Image-guided procedures, robotic interventions, and modeling, SPIE. pp. 174–182.

Nagy, T.D., Haidegger, T., 2019. A dvrk-based framework for surgical subtask automation. *Acta Polytechnica Hungarica* , 61–78.

Ni, Z.L., Bian, G.B., Wang, G.A., Zhou, X.H., Hou, Z.G., Chen, H.B., Xie, X.L., 2020. Pyramid attention aggregation network for semantic segmentation of surgical instruments, in: Proceedings of the AAAI Conference on Artificial Intelligence, pp. 11782–11790.

Ravi, N., Gabeur, V., Hu, Y.T., Hu, R., Ryali, C., Ma, T., Khedr, H., Rädle, R., Rolland, C., Gustafson, L., et al., 2024. Sam 2: Segment anything in images and videos. arXiv preprint arXiv:2408.00714 .

Ronneberger, O., Fischer, P., Brox, T., 2015. U-net: Convolutional networks for biomedical image segmentation, in: Medical Image Computing and Computer-Assisted Intervention–MICCAI 2015: 18th International Conference, Munich, Germany, October 5–9, 2015, Proceedings, Part III 18, Springer. pp. 234–241.

Shen, Y., Ding, H., Shao, X., Unberath, M., 2024. Performance and non-adversarial robustness of the segment anything model 2 in surgical video segmentation. arXiv preprint arXiv:2408.04098 .

Shvets, A.A., Raklin, A., Kalinin, A.A., Iglovikov, V.I., 2018. Automatic instrument segmentation in robot-assisted surgery using deep learning, in: 2018 17th IEEE international conference on machine learning and applications (ICMLA), IEEE. pp. 624–628.

Sun, X., Zou, Y., Wang, S., Su, H., Guan, B., 2022. A parallel network utilizing local features and global representations for segmentation of surgical instruments. *International Journal of Computer Assisted Radiology and Surgery* 17, 1903–1913.

Valderrama, N., Ruiz Puentes, P., Hernández, I., Ayobi, N., Verlyck, M., Santander, J., Caicedo, J., Fernández, N., Arbeláez, P., 2022. Towards holistic surgical scene understanding, in: International conference on medical image computing and computer-assisted intervention, Springer. pp. 442–452.

Watson, J., Aodha, O.M., Turmukhambetov, D., Brostow, G.J., Firman, M., 2020. Learning stereo from single images, in: Computer Vision–ECCV 2020: 16th European Conference, Glasgow, UK, August 23–28, 2020, Proceedings, Part I 16, Springer. pp. 722–740.

Wei, Y., Hu, H., Xie, Z., Zhang, Z., Cao, Y., Bao, J., Chen, D., Guo, B., 2022. Contrastive learning rivals masked image modeling in fine-tuning via feature distillation. Tech Report .

Zhao, Z., Jin, Y., Gao, X., Dou, Q., Heng, P.A., 2020. Learning motion flows for semi-supervised instrument segmentation from robotic surgical video, in: Medical Image Computing and Computer Assisted Intervention–MICCAI 2020: 23rd International Conference, Lima, Peru, October 4–8, 2020, Proceedings, Part III 23, Springer. pp. 679–689.

Zhao, Z., Jin, Y., Heng, P.A., 2022. Trasetr: track-to-segment transformer with contrastive query for instance-level instrument segmentation in robotic surgery, in: 2022 International Conference on Robotics and Automation (ICRA), IEEE. pp. 11186–11193.

Zhu, X., Su, W., Lu, L., Li, B., Wang, X., Dai, J., 2020. Deformable detr: Deformable transformers for end-to-end object detection. arXiv preprint arXiv:2010.04159 .

Zhu, X., Wang, Y., Dai, J., Yuan, L., Wei, Y., 2017. Flow-guided feature aggregation for video object detection, in: Proceedings of the IEEE international conference on computer vision, pp. 408–417.